HHS Public Access

Author manuscript

Int J Radiat Oncol Biol Phys. Author manuscript; available in PMC 2022 November 17.

Published in final edited form as:

Int J Radiat Oncol Biol Phys. 2018 August 01; 101(5): 1046–1056. doi:10.1016/j.ijrobp.2018.03.028.

Emerging Magnetic Resonance Imaging Technologies for Radiation Therapy Planning and Response Assessment

Kyle M. Jones, PhD[*,†], **Keith A. Michel, BS**[†], **James A. Bankson, PhD**[†], **Clifton D. Fuller, MD, PhD**[‡], **Ann H. Klopp, MD, PhD**[‡], **Aradhana M. Venkatesan, MD**[*]

[*]Section of Abdominal Imaging, Department of Diagnostic Radiology, Division of Diagnostic Imaging

[†]Department of Imaging Physics, Division of Diagnostic Imaging

[‡]Department of Radiation Oncology, Division of Radiation Oncology, MD Anderson Cancer Center, Houston, Texas

Abstract

Functional and molecular MRI techniques are capable of measuring biologic properties of tumor tissue. Knowledge of these biological properties may improve radiation treatment by more accurately identifying tumor volumes, characterizing radioresistant subvolumes of tumor before radiation therapy (RT), and identifying recurrent disease after RT. Intravoxel incoherent motion MRI, blood oxygenation level–dependent MRI, tissue oxygenation level–dependent MRI, hyperpolarized ^{13}C MRI, and chemical exchange saturation transfer MRI are relatively new MRI techniques that have shown promise for contributing to RT planning and response assessment. This review critically evaluates these emerging MR techniques, their potential role in RT planning, utility to date, and challenges to integration into the current clinical workflow.

Introduction

Anatomic MR images are increasingly integrated into radiation therapy (RT) planning, with published data demonstrating improvements in tumor delineation, dosimetry, and reduced toxicities compared with fluoroscopic, ultrasound, or CT-based planning (1). Limitations of conventional anatomic MRI are encountered when the morphologic appearance of residual or early recurrent disease overlaps with normal anatomy or treatment effects. Functional and molecular MR imaging techniques assess physiological parameters that are relevant to tumor biology, such as diffusion, perfusion, and oxygenation, and have the potential to overcome the limitations of conventional MRI. These techniques have the potential to improve detection of RT response and outcome and enable implementation of patient-tailored adaptive therapy regimens (2). Dynamic contrast-enhanced MRI (DCE MRI) and diffusion-weighted MRI (DW MRI) are well-known functional and molecular MRI techniques that

Reprint requests to: Aradhana M. Venkatesan, MD, Section of Abdominal Imaging, Department of Diagnostic Radiology, Division of Diagnostic Imaging, MD Anderson Cancer Center, 1400 Pressler St., Unit 1473, Houston TX 77030-4009. Tel: 713-563-8880; avenkatesan@mdanderson.org.

Conflict of interest: none.

have demonstrated success in RT response assessment, by interrogating changes in tissue perfusion and the Brownian motion of water molecules, respectively. Newer techniques, including intravoxel incoherent motion (IVIM) MRI, blood oxygenation level–dependent (BOLD) and tissue oxygenation level–dependent (TOLD) MRI, hyperpolarized ^{13}C MRI, and chemical exchange saturation transfer (CEST) MRI, permit noninvasive assessments of tissue properties that were previously impossible to evaluate. These assessments include the concomitant quantification of tissue water diffusion and perfusion in the absence of exogenous contrast agents, real-time assessments of blood and tissue oxygenation and tumor, and normal tissue glucose metabolism and protein concentration. Each of these properties is known to be altered in the setting of malignancy and as a result of RT. The focus of this article is to present a comprehensive review of these emerging MRI techniques, summarizing their potential clinical impact as well as the preclinical and clinical data relevant to potential RT planning, response assessment, and patient stratification.

Methods

A comprehensive search of the PubMed database was performed using the following imaging techniques: IVIM MRI, BOLD MRI, TOLD MRI, hyperpolarized ^{13}C MRI, and CEST MRI, in conjunction with the following terms: “radiation treatment,” “radiotherapy,” “radiation response assessment,” “radioresistance,” and “radiation treatment planning.” For each technique besides IVIM MRI, all published reports found through this search were included in this review. For IVIM MRI, priority was placed on summarizing the results of studies published within the past 5 years.

Emerging Functional MRI Techniques

IVIM MRI

Overview—Standard DW MRI and corresponding apparent diffusion coefficient (ADC) maps evaluate differences in the brownian motion of water caused by differences in tissue microstructure. Diffusion-weighted imaging and ADC images can therefore delineate areas of increased cellularity, as seen in sites of viable tumor (3). Standard ADC maps are acquired via a monoexponential approach, a relatively simple analytical approach relating signal attenuation to b value, that is unable to separate tissue diffusivity from microvascular perfusion (4, 5). Intravoxel incoherent motion MRI, developed by Le Bihan in the 1980s, uses a biexponential analytic approach, enabling the separation of perfusion-related parameters, including the pseudodiffusion coefficient (D*) and perfusion fraction (f), from tissue diffusivity parameters (ie, the pure diffusion coefficient [D]) (4, 5). As a result, concomitant information on both tissue perfusion and cell density can be derived non-invasively with IVIM imaging, without the administration of exogenous contrast agents as is required for traditional methods of perfusion assessment (eg, DCE MRI) (4-7).

For IVIM, multiple b values are used to acquire images at both low b values ≤ 100 s/mm^2 and high b values > 100 – 1000 s/mm^2. Signal attenuation is acquired at low b values associated with tissue diffusion and microcapillary perfusion as well as at high b values associated with only tissue diffusion. In well perfused tissue, the signal intensity versus b value shows steeper signal attenuation between points acquired with low b values compared

with points acquired with high b values. The data are then fit with a biexponential function with the assumption that signal attenuation observed is due to both tissue diffusion and capillary perfusion effects. A minimum of 4 b values is needed to estimate these metrics, although a larger number of b values are typically used to provide more precise estimations (8).

IVIM kinetics during RT and chemoradiotherapy—Intravoxel incoherent motion has been compared with more established techniques (eg, DCE MRI) for evaluating tumor perfusion during RT and chemoradiotherapy (CRT). In 23 metastatic lymph nodes of head and neck squamous cell carcinoma, Marzi et al (9) observed a positive relationship between the perfusion-related diffusion coefficient and semi-quantitative DCE parameters describing tissue perfusion (positive enhancement integral and maximum slope of increase). Hou et al (10) demonstrated in 43 nasopharyngeal carcinoma patients for whom water diffusivity, D, measured before CRT, had a higher area under the curve in receiver operating characteristic curve analysis than quantitative DCE analysis in the prediction of short-term responses to CRT. Gaeta et al (11) demonstrated a significant change in initial area under the curve (measured with DCE MRI) and D* over time in response to RT in 15 lytic bone metastases from breast cancer. These studies suggest that perfusion-related and non–perfusion-related diffusion coefficients are similar to or superior to DCE-derived parameters in evaluating perfusion during RT in a variety of cancer types.

Multiple studies have compared IVIM-derived diffusion and perfusion measurements and traditional ADC measurements to predict and monitor response to RT and CRT. Marzi et al (12) showed that pretreatment D and f parameters derived with IVIM were superior to ADC in predicting the relative shrinkage of irradiated salivary gland in 34 patients with head and neck cancer. Lai et al (13) showed that D and f values were significantly lower in nasopharyngeal carcinoma versus postchemoradiotherapy fibrosis, whereas ADC values were not significantly different in 53 patients. Other studies have shown that water diffusivity as measured with IVIM and traditional monoexponential analysis is similar in evaluating RT response. Additionally, these studies have shown that water diffusivity measurements are more helpful than perfusion-related diffusion coefficients (D* and f) derived from IVIM in assessing RT response. Nougaret et al (14) showed that median D and ADC values obtained after CRT in 31 patients with rectal cancer were useful in discriminating good versus poor responders to RT, as assessed by histopathology, but D* and f were not. Xiao-ping et al (15) showed that pretreatment ADC, pretreatment D, and change in %D could successfully discriminate nasopharyngeal carcinoma patients who would have complete response to CRT from those who would have a partial response, with response defined by volume of residual tumor at the end of the study. These findings suggest that diffusion-related IVIM parameters may be more predictive than perfusion-related IVIM parameters in evaluating RT response in certain cancer types.

BOLD and TOLD MRI

Overview—Tumor hypoxia, which has been associated with tumor aggressiveness and radioresistance, can be measured non-invasively with BOLD/TOLD MRI techniques (16). Blood oxygen level–dependent MRI measures hypoxia through signal loss in tissue

because of paramagnetic deoxygenated red blood cells, which generate local magnetic field gradients (17). Tissue oxygenation level–dependent MRI distinguishes oxygenated tissue from hypoxic tissue through a signal increase in oxygenated tissue because of the absence of paramagnetic deoxyhemoglobin. These effects are detected by acquiring spin–spin relaxation time (T_2*) and spin–lattice relaxation time (T_1) measurements, respectively.

Blood oxygenation level–dependent imaging typically involves the use of a T_2-weighted gradient echo with a multi-echo sequence. Tissue oxygenation level–dependent imaging involves acquiring multiple T_1-weighted images. T_2* is measured by fitting an exponential function to the multi-echo data with respect to the echo time. Similarly, T_1 is measured by fitting an exponential function to the T_1-weighted image data with respect to the repetition time. In many BOLD and TOLD MRI experiments, MRI sequences are performed before and after an oxygen challenge (Fig. 1A). The change in T_2* or T_1 before and after hyperoxic challenge is used as a measure of hypoxia, with normoxic tissue showing a larger change in T_2* and T_1 compared with hypoxic tissue (Fig. 1B). Differentiating normoxic from hypoxic tissue can potentially be beneficial in generating a treatment plan because a lower dose of radiation will likely be used for normoxic tissue relative to hypoxic tissue.

Blood oxygenation level–dependent/TOLD MRI measurements correlate with direct measures of tissue oxygenation. Zhao et al (18) described a significant correlation between mean tumor partial pressure of oxygen (pO_2) measurements made with ^{19}F MRI oximetry and the change in mean T_2* values after hyperoxic challenge in rat 13762NF breast carcinomas. O'Connor et al (17) observed a correlation between DCE MRI and TOLD MRI in 10 patients with locally advanced or metastatic disease within the abdomen and/or pelvis. Here, moderate uptake of gadolinium (moderate perfusion) was associated with a small change in T_1 after hyperoxic challenge (low oxygen concentration), indicating that DCE MRI and TOLD MRI can be used together to identify hypoxic tissue (19).

BOLD and TOLD as a predictor of response to RT and CRT—Several preclinical studies have compared the ability of BOLD and TOLD MRI to predict and monitor response to RT. White et al (20) examined 25 Dunning R3327-AT1 prostate tumors in a rat model and showed that tumors with a large TOLD response (ΔR_1) after hyperoxic challenge before radiation treatment (normoxic tissue) had a significant growth delay compared with tumors that had a low TOLD response before treatment (hypoxic tissue). Hallac et al (21) showed similar results in the same tumor model, emphasizing the potential importance of pretreatment TOLD MRI measurements in prostrate tumors in RT. Zhou et al (22) demonstrated the ability of BOLD MRI to detect RT effects in a preclinical lung cancer model shortly after treatment. Dynamic contrast-enhanced MRI was also used to assess response to RT and interestingly showed minimal changes, suggesting BOLD MRI may be more helpful in monitoring response to RT in lung cancer. Similarly, Lin et al (23) showed a decrease in ΔT_2* in TRAMP-C1 (adenocarcinoma of mouse prostate) tumors after RT, whereas untreated tumors showed no changes ΔT_2*.

Clinical studies have shown that BOLD and/or TOLD are sensitive to hyperoxic gas challenge in patients with breast, brain, cervix, prostate, liver, and head and neck cancer

(24-29). Clinical translation of BOLD/TOLD to predict radiation response in patients is expected in the future (30).

Hyperpolarized ^{13}C MRI

Overview—Dysregulated metabolism is a hallmark of malignancies and associated with poor prognosis. Potential benefits of imaging cancer metabolism in vivo include the potential to provide information concerning pretreatment tumor aggressiveness, to detect modulations in metabolism at early stages after therapy, and to elucidate metabolic signatures associated with responder status to improve patient stratification and prognostication (31-33). Magnetic resonance spectroscopy has been used to measure metabolite concentrations in vivo, but sensitivity is poor and only molecules with hydrogen can be imaged. Hyperpolarization increases the MR signal intensity of MR-visible nuclei by a factor of 10,000 or more and thereby greatly improves detection sensitivity, which allows for molecules other than hydrogen, like ^{13}C, to be imaged (34).

The majority of literature on hyperpolarized MRI in cancer has used ^{13}C-pyruvate, given its sufficiently long T1 relaxation time and the central role of pyruvate in metabolism and aerobic glycolysis (32). Other substrates that have been successfully hyperpolarized include ^{13}C-fumarate, which has been studied as a marker of cell necrosis (35, 36), ^{13}C-bicarbonate as a measure of pH (36, 37), and ^{13}C-urea as a marker of perfusion (36). ^{13}C-pyruvate and its byproduct in aerobic glycolysis, ^{13}C-lactate, serve as markers for dysregulated metabolism. Contrary to normal differentiated cells, which rely on mitochondrial oxidative phosphorylation to produce adenosine triphosphate (ATP), cancer cells produce ATP less efficiently through enhanced aerobic glycolysis, and the glycolytic intermediates formed can be used to generate energy substrates needed for rapid proliferation (38). The end product of aerobic glycolysis is lactate, which is not formed during mitochondrial oxidative phosphorylation. Thus, monitoring hyperpolarized ^{13}C-pyruvate consumption and hyperpolarized ^{13}C-lactate accumulation in tumors after injection of hyperpolarized ^{13}C-pyruvate allows for lactate fractions and apparent pyruvate-to-lactate conversion rates to be measured, which have been shown to differentiate high- versus low-grade tumors and tumor versus necrotic tissue (39).

In vivo metabolic imaging by MRI has historically been limited by poor signal-to-noise ratio. Dynamic nuclear polarization is a technique that permits significant (>10,000-fold) improvements in sensitivity, making nuclear MRI a viable method to evaluate metabolic conversions in real time. Dynamic nuclear polarization is the method most widely used to enhance spin polarization, including in initial clinical trials. This method transfers the nuclear spin state of highly polarized electrons to nuclei. Once polarized, ^{13}C-pyruvate has an approximate 30- to 40-second half-life after it leaves the dynamic nuclear polarization polarizer, with its detectable MR signal lasting for a few minutes. Thus, injection of the hyperpolarized agent, uptake of the agent by the tissue of interest, and metabolism of the agent must occur rapidly. Fast imaging sequences with low tip angle excitation pulses are typically used to maximize dynamic information obtained and minimize signal loss (40). Analysis methods to measure pyruvate-to-lactate conversion rates require a pharmacokinetic model that accounts for delivery, the transient nature of the signal, and variation in spatial

distribution of nuclei over time (41). Recent work at our institution demonstrates typical data outputs in a hyperpolarized ^{13}C-pyruvate experiment, with pyruvate and lactate signal recorded after injection and a time averaged spectrum used to calculate lactate fractions in a clinically relevant human papillomavirus–associated gynecologic cancer model (Fig. 2, Video 1).

Hyperpolarized ^{13}C-pyruvate MRI as a predictor of response to RT— Hyperpolarized ^{13}C MRI is a relatively new technique and requires complicated imaging acquisitions and analytic techniques, as well as an instrument that can perform hyperpolarization. As such, there are limited preclinical studies that have examined hyperpolarized ^{13}C MRI for RT response and no known clinical studies to date. The existing preclinical studies are discussed.

Sandulache et al (42) demonstrated an acute drop in the conversion rate of ^{13}C-pyruvate to ^{13}C-lactate after RT in a preclinical model of anaplastic thyroid cancer (42). The drop in conversion rate was confirmed ex vivo to correspond to decreased concentrations of reducing equivalents in tumor. Because tumor cells use reducing equivalents to neutralize reactive oxygen species, which mediate ionizing radiation cytotoxicity, a reduction in the reducing potential of tumors is indicative of treatment response. Day et al (43) investigated the ability of hyperpolarized ^{13}C-pyruvate MRI to detect treatment response to RT in a glioma tumor model. High levels of lactate were observed in tumor compared with surrounding brain, with a 34% decrease in the measured tumor lactate fraction detectable 72 hours after whole-brain radiation with 15 Gy. Saito et al (44) observed a significant decrease in lactate fraction measurements immediately after RT relative to before treatment in squamous cell carcinoma (SCCVII) and colon cancer (HT-29) tumors implanted subcutaneously in mice. These preclinical studies suggest that hyperpolarized ^{13}C-pyruvate MRI may serve as a useful biomarker to evaluate radiation treatment effects at early time points.

Chemical exchange saturation transfer

Overview—Chemical exchange saturation transfer MRI indirectly measures mobile protein and peptide content in tissue. Protein content is higher in areas of increased cellular density and proliferation, which may be increased in rapidly proliferating tumors. This imaging approach may be informative to monitor early effects of RT, which results in destruction of the cytoplasm, increasing the mobile protein content. Decreases in mobile protein content with CEST MRI may, in fact, be observed at earlier time points than decreases in tissue cellularity assessed with DW MRI.

Chemical exchange saturation transfer (CEST) detects endogenous biomolecules that possess protons that can undergo exchange with water molecules (45, 46). Endogenous biomolecules include amide protons of mobile proteins (amide proton transfer [APT] MRI) (47), amine protons of mobile proteins (amine CEST) (48), glycosaminoglycans (49), glutamate (50), creatine (51), and lactate (52). Evidence suggests that viable solid tumors have higher concentrations of mobile proteins and peptides than normal tissue, thus tumors generate higher contrast with APT and amine CEST MRI relative to normal tissue 53-56

(Fig. 3). Amide proton transfer MRI findings have been associated with tumor grade as assessed by histopathology, with decreases in CEST signal intensity observed as a result of therapy (57-59). Amine CEST MRI has also shown promise in detecting tumor response to therapy in the preclinical setting (60).

Chemical exchange saturation transfer imaging is acquired by applying a radiofrequency saturation pulse at the resonant frequency of a proton on the biomolecule of interest that can exchange with protons on water molecules. The saturation pulse destroys the signal from the exchangeable proton, after which the proton exchanges with water and causes a loss in the water signal (Fig. 4). Imaging typically involves acquiring proton density–weighted images using a range of saturation frequencies. A CEST spectrum can then be generated by plotting water signal intensity versus MR saturation frequency.

CEST as a predictor of response to RT—Ma et al (61) used APT MRI to distinguish true progression from pseudoprogression in glioma patients who received radiation treatment (61). Necrosis and inflammation are common side effects of radiation treatment and can sometimes be mistaken as recurrent tumor on standard T_2-weighted and gadolinium-enhanced MR scans (pseudoprogression). In this study, patients later diagnosed with true progression demonstrated hyperintense tumor APT signal intensities, whereas patients later diagnosed with pseudoprogression showed isointense to mildly hyperintense tumor APT signal intensities (Fig. 5). Similar results were seen in a preclinical glioma model (62), corroborating the assumption that RT results in the destruction of the cytoplasm, which is rich in mobile protein content, thus causing a decrease in APT signal intensity

Clinical studies of CEST MRI have been used in multiple research centers worldwide (63), but the ability of CEST MRI to predict and evaluate RT response is currently limited to the single glioma study by Ma et al described (61). More studies are expected in the near future, given the clinical feasibility of CEST MRI acquisitions and analytical techniques.

Planning Considerations for Functional MR-Guided RT

The prospect of greater multiparametric MRI integration into RT planning poses several challenges. At present, CT remains the primary imaging modality used for clinical RT planning, with CT-based calculations of the mass attenuation coefficient being critical for precise radiation dose calculation (64). Magnetic resonance imaging is unable to calculate the mass attenuation coefficient with the same accuracy as CT, although advances have been made to address this problem by providing more accurate estimations for the necessary electron density information (65, 66). Magnetic resonance imaging offers unique advantages given its superior soft tissue contrast relative to CT. The development of MR–linear accelerator (MR-Linac) systems offering real-time MRI of tumor locations during treatment delivery is expected to facilitate greater real-time MR-based RT planning and execution, with the potential to improve the identification of radiosensitive areas and better sculpt dose to the planning target volume, thus widening the therapeutic window (67). Modulation of dose according to user specifications allows for escalated dose to tumor while maintaining consistent minimal dose to organs at risk. Existing technical challenges inherent to the MR-Linac include the lack of electron density data obtained, which limits the measurement

accuracy of dose calculation (68). In addition, secondary electrons caused by the magnetic field within the MR-Linac influence RT dose distribution. These issues are being addressed during the development of the MR-Linac, with strategies including a real-time Monte Carlo approach to account for the influence of the magnetic field on dose calculation (69).

Potential Roles of Functional and Molecular MRI for Adaptive Therapy Planning

At present, MRI-based dose modifications can be challenging to implement, particularly early in the course of RT as the tumor microenvironment is affected by hypoxia, granulation tissue, and edema, with both residual tumor and radiation fibrosis appearing as areas of increased signal on T_2-weighted images. Biological feedback derived from functional imaging may make it possible to identify viable tumor from radiation effects. Adaptive RT could alter the treatment plan to account for functional changes to the target volume and organs at risk. The ability to adapt according to the information derived from functional imaging, particularly if this feedback precedes morphologic changes, may enable patient-specific dose escalation, thus improving treatment accuracy and reducing toxicities (70). Adaptive RT studies have not been investigated with IVIM, BOLD/TOLD MRI, CEST MRI, or hyperpolarized ^{13}C MRI to date, but it is noted that these methods have unique advantages compared with more well-studied techniques, like DW MRI and DCE MRI. They either require no contrast injection (IVIM, BOLD/TOLD, APT MRI) or entail injection of a physiological substance (hyperpolarized MRI), making them suitable for repeated use during multiple RT sessions. Additionally, many of these newer techniques measure unique biomarkers relevant to RT that cannot be measured with other techniques. Blood oxygen level–dependent MRI and TOLD MRI measure pixelwise tumor oxygenation levels, potentially offering clinicians the ability to increase the radiation dose to hypoxic pixels relative to normoxic pixels. Intravoxel incoherent motion measures tissue perfusion at the capillary level without administration of contrast, offering an advantage over contrast-based tissue perfusion measurements acquired with DCE MRI. Chemical exchange saturation transfer and hyperpolarized ^{13}C-MRI measure mobile protein content and dysregulated energy metabolism, respectively. These biomarkers may enable assessment of RT efficacy at earlier time points compared with existing MR techniques. At present, clinically available MR techniques such as DW imaging may not demonstrate changes in ADC until several weeks to months after treatment (71).

Challenges Related to Use of Functional MRI for RT Guidance

Anatomic CT and MRI scans produce high spatial resolution images of 1 to 2 mm^3. Functional MR images are typically acquired with lower spatial resolution (Table 1). This is especially true in the case of hyperpolarized ^{13}C-pyruvate MRI, which has a short 30- to 40-second half-life that requires fast imaging sequences, sacrificing spatial resolution and the number of slices that can be collected. In fact, many preclinical hyperpolarized ^{13}C studies collect data from a single slice without spatial information. Low spatial resolution images are difficult to co-register with anatomic MR/CT images, thus complicating RT target definition. As such, hyperpolarized MRI may be more suitable in assessing RT

response than for the development of a multi-voxel treatment plan. Chemical exchange saturation transfer and BOLD/TOLD MRI techniques provide images at spatial resolutions comparable to anatomic MRI scans, with the potential to guide voxel level dose delivery.

Intravoxel incoherent motion MRI and BOLD MRI data acquire images purely from water molecules and therefore can be easily performed at clinically relevant field strengths (1.5-3 T). Hyperpolarized MRI and CEST MRI rely on acquiring signal from small pools of endogenous and exogenous biomolecules and therefore benefit significantly from higher field strengths. In fact, many clinical CEST MRI studies of exogenous molecules are performed at 7 T owing to the increase in signal obtained, as well as the more selective saturation of exogenous molecules that is offered at 7 T compared with 3 T. Technical advancements are anticipated for CEST and hyperpolarized MRI techniques to increase detection sensitivity so that they can be performed routinely at lower field strengths, thus broadening their applicability across practice settings.

Geometric distortions in images caused by magnetic field inhomogeneity or MR gradient coil nonlinearity also complicate the integration of advanced functional imaging techniques for RT planning. If the distortion is intrinsic to the scanner itself, the distortion can be corrected for through modeling or by insertion of a non-uniform object. However, patient-induced geometric distortions, which are typical in the lung and head and neck regions, cannot be corrected. Patient motion can also compromise MR tumor localization. For targeted RT, extensive care needs to be taken to ensure the dose is delivered precisely and accurately. Thus, sufficient correction algorithms are needed for MR images acquired in parts of the body commonly associated with geometric and motion distortion.

Quantification methods to generate parametric maps are challenging for many functional and molecular MR techniques. For example, DCE MRI and hyperpolarized MRI often use complex pharmacokinetic models to measure functional parameters, which increase postprocessing time and can be difficult to replicate precisely because they are often user-intensive. Differences in procedural and postprocessing techniques have led to large differences in parameter estimations between studies. Thus, standardized acquisition and quantitative analysis methods need to be determined for certain functional MR techniques to improve robustness. Furthermore, visual interpretation of parametric maps is greatly influenced by the threshold chosen. For example, the perception of tumor size or the degree of aggressiveness of the tumor can be changed drastically by simply changing the maximum value of the parametric map. Because interpretation of some functional parameters, like K^{trans} in DCE MRI, is still uncertain, guidance for thresholds is lacking and thus left largely to the discretion of the individual analyzing the data.

The optimal timing to acquire functional images for RT planning/monitoring is currently unknown and remains an area of investigation. Because cancer metabolism, tumor cell proliferation, and hypoxia are expected to change significantly throughout treatment, it will be important to determine exactly when and how often functional MR techniques should be used. In addition to timing, interpretation can become difficult if functional MR maps provide conflicting information. In past studies, support vector machine or

logistic regression models have been used to increase confidence in the interpretation of multiparametric information (73-75).

Scanning time costs remain barriers to widespread integration of functional MRI for RT planning. Many CEST MRI techniques require long scan times because of the necessity of applying long saturation periods before each image acquisition and acquiring multiple images to obtain a CEST spectrum. Blood oxygen level–dependent MRI requires multiple scans when acquiring images with and without a hyperoxic challenge. Hyperpolarized MR acquisitions are short (roughly 3 minutes), but they depend on successful polarization of an agent, which requires sufficient time (roughly 1 hour for ^{13}C-pyruvate) and therefore could cause a long scan time if the polarization process and the beginning of MR acquisitions are not timed properly. Increased scan time leads to increased cost as well as increased patient discomfort during scanning, which can lead to image registration issues between functional MR images and anatomic MR images as a result of movement in between scans. Several strategies are being developed to circumvent these limitations. Examples include the development of fast 3-dimensional gradient echo sequences for CEST MRI that significantly shorten multi-slice CEST MRI acquisition times. Additionally, advanced parallel imaging methods, which can be applied to most MRI techniques, including CEST and BOLD/TOLD MRI, are being developed to increase MR scan acquisition speeds by reducing the number of phase-encoding steps collected during imaging (76).

Conclusions

Recently developed functional and molecular MR techniques offer unique means of assessing tumor perfusion, cell density, hypoxia, and metabolism and thus have the potential for translational applications in adaptive treatment planning, prediction of outcome, and monitoring of treatment response. Diffusion-weighted imaging, DCE MRI, and MR spectroscopy have shown promise in predicting and monitoring response to RT. Blood oxygen level–dependent, TOLD, CEST, and hyperpolarized MRI are newer techniques that have been explored primarily in the preclinical setting and in a finite number of clinical studies, which have shown promise in providing additional functional detail relevant to RT planning and response assessment. Integration of functional and molecular MR techniques into current radiation treatment workflow will necessitate overcoming technical limitations, including low spatial/temporal resolution and the need for standardization of methods. Continued maturation of these techniques is anticipated, with optimization and standardization of protocols and the development of image analysis algorithms capable of accounting for intratumoral heterogeneity and changes in intratumoral MR signal during therapy. Additional advances are anticipated to combine functional MR and positron emission tomography parameters, which may have a role in RT planning and assessment in the future (77). Reproducibility across sites should be ensured to facilitate clinical translation of these technologies. Working groups are in the process of developing standardized methods and guidelines for acquisition, optimization, analysis, and quality assurance. Prospective multicenter clinical studies will be necessary to define the specific clinical benefits of these techniques by patient population and histologic subtype in terms of optimum dosimetry, dose reduction, reduced toxicities, and survival.

Supplementary Material

Refer to Web version on PubMed Central for supplementary material.

Acknowledgment

The authors thank Dr R. Jason Stafford, PhD, for advice in composing Table 1.

Research described in this review and performed by the authors was supported by grant support from Toshiba America Medical Systems, the RSNA Research and Education Foundation, the National Cancer Institute (P30-CA016672), and by institutional funds from the University of Texas MD Anderson Cancer Center.

References

1. Dawson LA, Menard C. Imaging in radiation oncology: A perspective. Oncologist 2010;15:338–349. [PubMed: 20413639]
2. Gladwish A, Han K. Novel imaging for treatment planning or tumor response. In: Tofilon P, Camphausen K, editors. Increasing the Therapeutic Ratio of Radiotherapy. Cancer Drug Discovery and Development. New York: Humana Press; 2017.
3. Padhani AR. Diffusion magnetic resonance imaging in cancer patient management. Semin Radiat Oncol 2011;21:119–140. [PubMed: 21356480]
4. Ding Y, Hazle JD, Mohammed AS, et al. Intravoxel incoherent motion imaging kinetics during chemoradiotherapy for human papillomavirus-associated squamous cell carcinoma of the oropharynx: Preliminary results from a prospective pilot study. NMR Biomed 2015;28:1645–1654. [PubMed: 26451969]
5. Le Bihan D, Breton E, Lallemand D, et al. MR imaging of intravoxel incoherent motions: Application to diffusion and perfusion in neurologic disorders. Radiology 1986;161:401–407. [PubMed: 3763909]
6. Le Bihan D, Breton E, Lallemand D, et al. Separation of diffusion and perfusion in intravoxel incoherent motion MR imaging. Radiology 1988;168:497–505. [PubMed: 3393671]
7. Le Bihan D Intravoxel incoherent motion perfusion MR imaging: A wake-up call. Radiology 2008;249:748–752. [PubMed: 19011179]
8. Koh DM, Collins DJ, Orton MR. Intravoxel incoherent motion in body diffusion-weighted MRI: Reality and challenges. AJR Am J Roentgenol 2011;196:1351–1361. [PubMed: 21606299]
9. Marzi S, Piludu F, Forina C, et al. Correlation study between intravoxel incoherent motion MRI and dynamic contrast-enhanced MRI in head and neck squamous cell carcinoma: Evaluation in primary tumors and metastatic nodes. Magn Reson Imaging 2017;37:1–8. [PubMed: 27742432]
10. Hou J, Yu X, Hu Y, et al. Value of intravoxel incoherent motion and dynamic contrast-enhanced MRI for predicting the early and short-term responses to chemoradiotherapy in nasopharyngeal carcinoma. Medicine (Baltimore) 2016;95:e4320. [PubMed: 27583847]
11. Gaeta M, Benedetto C, Minutoli F, et al. Use of diffusion-weighted, intravoxel incoherent motion, and dynamic contrast-enhanced MR imaging in the assessment of response to radiotherapy of lytic bone metastases from breast cancer. Acad Radiol 2014;21:1286–1293. [PubMed: 25088834]
12. Marzi S, Forina C, Marucci L, et al. Early radiation-induced changes evaluated by intravoxel incoherent motion in the major salivary glands. J Magn Reson Imaging 2015;41:974–982. [PubMed: 24700435]
13. Lai V, Li X, Lee VH, et al. Intravoxel incoherent motion MR imaging: Comparison of diffusion and perfusion characteristics between nasopharyngeal carcinoma and post-chemoradiotherpy fibrosis. Eur Radiol 2013;23:2793–2801. [PubMed: 23722897]
14. Nougaret S, Vargas HA, Lakhman Y, et al. Intravoxel incoherent motion-derived histogram metrics for assessment of response after combined chemotherapy and RT in rectal cancer: Initial experience and comparison between single-section and volumetric analyses. Radiology 2016;280:446–454. [PubMed: 26919562]

15. Xiao-ping Y, Jing H, Fei-ping L, et al. Intravoxel incoherent motion MRI for predicting early response to induction chemotherapy and chemoradiotherapy in patients with nasopharyngeal carcinoma. J Magn Reson Imaging 2016;43:1179–1190. [PubMed: 26540374]
16. Overgaard J. Hypoxic radiosensitization: Adored and ignored. J Clin Oncol 2007;25:4066–4074. [PubMed: 17827455]
17. Young IR, Clarke GJ, Bailes DR, et al. Enhancement of relaxation rate with paramagnetic contrast agents in NMR imaging. J Comput Tomogr 1981;5:543–547. [PubMed: 7053127]
18. Zhao D, Lan JL, Hahn EW, et al. Comparison of ^{1}H blood oxygen level-dependent (BOLD) and ^{19}F MRI to investigate tumor oxygenation. Magn Reson Med 2009;62:357–364. [PubMed: 19526495]
19. O'Connor JPB, Naish JH, Parker GJM, et al. Preliminary study of oxygen-enhanced longitudinal relaxation in MRI: A potential novel biomarker of oxygenation changes in solid tumors. Int J Radiat Oncol Biol Phys 2009;75:1209–1215. [PubMed: 19327904]
20. White DA, Zhang Z, Li L, et al. Developing oxygen-enhanced magnetic resonance imaging as a prognostic biomarker of radiation response. Cancer Lett 2016;380:69–77. [PubMed: 27267808]
21. Hallac RR, Zhou H, Pidikiti R, et al. Correlations of noninvasive BOLD and TOLD MRI with pO2 and relevance to tumor radiation response. Magn Reson Med 2014;71:1863–1873. [PubMed: 23813468]
22. Zhou H, Zhang Z, Denney R, et al. Tumor physiological changes during hypofractionated stereotactic body radiation therapy assessed using multi-parametric magnetic resonance imaging. Oncotarget 2017;8:37464–37477. [PubMed: 28415581]
23. Lin YC, Wang JJ, Hong JH, et al. Noninvasive monitoring of microvascular changes with partial irradiation using dynamic contrast-enhanced and blood oxygen level-dependent magnetic resonance imaging. J Radiat Oncol Biol Phys 2013;85:1367–1374.
24. Penner RR, Daniel B, Glover GH. Detecting blood oxygen level-dependent (BOLD) contrast in the breast. J Magn Reson Imaging 2010;32:120–129. [PubMed: 20578018]
25. Linnik IV, Scott MLJ, Holliday KF. Noninvasive tumor hypoxia measurement using magnetic resonance imaging in murine U87 glioma xenografts and in patients with glioblastoma. Magn Reson Med 2014;71:1854–1862. [PubMed: 23798369]
26. Hallac RR, Ding Y, Yuan Q, et al. Oxygenation in cervical cancer and normal uterine cervix assessed using blood oxygenation level-dependent (BOLD) MRI at 3T. NMR Biomed 2012;25:1321–1330. [PubMed: 22619091]
27. Alonzi R, Padhani AR, Maxwell RJ, et al. Carbogen breathing increases prostate cancer oxygenation: A translational MRI study in murine xenografts and humans. Br J Cancer 2009;100:644–648. [PubMed: 19190629]
28. Patterson AJ, Priest AN, Bowden DJ, et al. Quantitative BOLD imaging at 3T: Temporal changes in hepatocellular carcinoma and fibrosis following oxygen challenge. J Magn Reson 2016;44:739–744.
29. Rijpkema M, Kaanders JH, Joosten FB, et al. Effects of breathing a hyperoxic hypercapnic gas mixture on blood oxygenation and vascularity of head and-neck tumors as measured by magnetic resonance imaging. Int J Radiat Oncol Biol Phys 2002;53:1185–1191. [PubMed: 12128119]
30. Rumley CN, Lee MT, Holloway L, et al. Multiparametric magnetic resonance imaging in mucosal primary head and neck cancer: A prospective imaging biomarker study. BMC Cancer 2017;17:475. [PubMed: 28693449]
31. Chen HY, Larson PEZ, Bok RA, et al. Assessing prostate cancer aggressiveness with hyperpolarized dual-agent 3D dynamic imaging of metabolism and perfusion. Cancer Res 2017;17:3207–3216.
32. Day SE, Kettunen MI, Gallagher FA, et al. Detecting tumor response to treatment using hyperpolarized 13C magnetic resonance imaging and spectroscopy. Nat Med 2007;13:1382–1387. [PubMed: 17965722]
33. Keshari KR, Wilson DM, Van Criekinge M, et al. Metabolic response of prostate cancer to nicotinamide phophoribosyltransferase inhibition in a hyperpolarized MR/PET compatible bioreactor. Prostate 2015;75:1601–1609. [PubMed: 26177608]

34. Ardenkjaer-Larsen JH, Fridlund B, Gram A, et al. Increase in signal-to-noise ratio of > 10,000 times in liquid-state NMR. Proc Natl Acad Sci U S A 2003;100:10158–10163. [PubMed: 12930897]
35. Gallagher FA, Kettunen MI, Hu DE, et al. Production of hyperpolarized [1,4-13C2]malate from [1,4-13C2]fumarate is a marker of cell necrosis and treatment response in tumors. Proc Natl Acad Sci U S A 2009;106:19801–19806. [PubMed: 19903889]
36. Wilson DM, Keshari KR, Larson PE, et al. Multi-compound polarization by DNP allows simultaneous assessment of multiple enzymatic activities in vivo. J Magn Reson 2010;205:141–147. [PubMed: 20478721]
37. Gallagher FA, Kettunen MI, Day SE, et al. Magnetic resonance imaging of pH in vivo using hyperpolarized 13C-labelled bicarbonate. Nature 2008;453:940–943. [PubMed: 18509335]
38. Vander Heiden MG, Cantley LC, Thompson CB. Understanding the Warburg effect: The metabolic requirements of cell proliferation. Science 2009;324:1029–1033. [PubMed: 19460998]
39. Albers MJ, Bok R, Chen AP, et al. Hyperpolarized 13C lactate, pyruvate, and alanine: Noninvasive biomarkers for prostate cancer detection and grading. Cancer Res 2008;68:8607–8615. [PubMed: 18922937]
40. Mayer D, Yen YF, Levin YS, et al. In vivo application of sub-second spiral chemical shift imaging (CSI) to hyperpolarized 13C metabolic imaging: Comparison with phase-encoded CSI. J Magn Reson 2010;204:340–345. [PubMed: 20346717]
41. Bankson JA, Walker CM, Ramirez MS, et al. Kinetic modeling and constrained reconstruction of hyperpolarized [1-13C]-pyruvate offers improved metabolic imaging of tumors. Cancer Res 2015;75:4708–4717. [PubMed: 26420214]
42. Sandulache VC, Chen Y, Lee J, et al. Evaluation of hyperpolarized [1-^{13}C]-pyruvate by magnetic resonance to detect ionizing radiation effects in real time. PLoS One 2014;9:e87031. [PubMed: 24475215]
43. Day SE, Kettunen MI, Cherukuri MK, et al. Detecting response of rat C6 glioma tumors to RT using hyperpolarized [1-13C]pyruvate and ^{13}C magnetic resonance spectroscopic imaging. Magn Reson Med 2011;65:557–563. [PubMed: 21264939]
44. Saito K, Matsumoto S, Takakusagi Y, et al. 13C-MR spectroscopic imaging with hyperpolarized [1-13C]pyruvate detects early response to radiotherapy in SCC tumors and HT-29 tumors. Clin Cancer Res 2015;21:5073–5081. [PubMed: 25673698]
45. Ward KM, Aletras AH, Balaban RS. A new class of contrast agents for MRI based on proton chemical exchange dependent saturation transfer (CEST). J Magn Reson 2000;143:79–87. [PubMed: 10698648]
46. van Zijl PCM, Yadav NN. Chemical exchange saturation transfer (CEST): What is in a name and what isn't? Magn Reson Med 2011;65:927–948. [PubMed: 21337419]
47. Tietze A, Blicher J, Mikkelsen IK, et al. Assessment of ischemic penumbra in patients with hyperacute stroke using amide proton transfer (APT) chemical exchange saturation transfer (CEST) MRI. NMR Biomed 2014;27:163–174. [PubMed: 24288260]
48. Harris RJ, Cloughesy TF, Liau LM, et al. pH-weighted molecular imaging of gliomas using amine chemical exchange saturation transfer MRI. Neuro Oncol 2015;17:1514–1524. [PubMed: 26113557]
49. Lee YH, Yang J, Jeong HK, et al. Assessment of the patellofemoral cartilage: Correlation of knee pain score with magnetic resonance cartilage grading and magnetization transfer ratio asymmetry of glycosaminoglycan chemical exchange saturation transfer. Magn Reson Imaging 2016;35:61–68. [PubMed: 27580516]
50. Davis KA, Nanga RP, Das S, et al. Glutamate imaging (GluCEST) lateralizes epileptic foci in nonlesional temporal lobe epilepsy. Sci Transl Med 2015;7:309ra161.
51. Kogan F, Haris M, Debrosse C, et al. In vivo chemical exchange saturation transfer of creatine (CrCEST) in skeletal muscle at 3 T. J Magn Reson Imaging 2014;40:596–602. [PubMed: 24925857]
52. DeBrosse C, Prakash R, Nanga R, et al. Lactate chemical exchange saturation transfer (LATEST) imaging in vivo: A biomarker for LDH activity. Sci Rep 2016;6:19517. [PubMed: 26794265]

53. Wen Z, Hu S, Huang F, et al. MR imaging of high-grade brain tumors using endogenous protein and peptide-based contrast. Neuroimage 2010;51:616–622. [PubMed: 20188197]
54. Yan K, Fu Z, Yang C, et al. Assessing amide proton transfer (APT) MRI contrast origins in 9 L gliosarcoma in the rat brain using proteomic analysis. Mol Imaging Biol 2015;17:479–487. [PubMed: 25622812]
55. Zhou J, Yan K, Zhu H. A simple model for understanding the origin of the amide proton transfer MRI signal in tissue. Applied Magn Reson 2012;42:393–402.
56. Zhou J, Zhu H, Lim M, et al. Three-dimensional amide proton transfer MR imaging of gliomas: Initial experience and comparison with gadolinium enhancement. J Magn Reson Imaging 2013;38: 1119–1128. [PubMed: 23440878]
57. Togao O, Yoshiura T, Keupp J, et al. Amide proton transfer imaging of adult diffuse gliomas: Correlation with histopathological grades. Neuro Oncol 2014;16:441–448. [PubMed: 24305718]
58. Blakeley JO, Ye X, Lim M, et al. The role of amide proton transfer imaging in detecting active malignant glioma. J Clin Oncol 2011;29: 2024.
59. Park KJ, Kim HS, Park JE, et al. Added value of amide proton transfer imaging to conventional and perfusion MR imaging for evaluating the treatment response of newly diagnosed glioblastoma. Euro Radiol 2016;26:4390–4403.
60. Marathe K, McVicar N, Li A, et al. Topiramate induces acute intracellular acidification in glioblastoma. J Neurooncol 2016;130: 465–472. [PubMed: 27613534]
61. Ma B, Blakeley JO, Hong X, et al. Applying amide proton transfer-weighted MRI to distinguish pseudoprogression from true progression in malignant gliomas. J Magn Reson Imaging 2016;44: 456–462. [PubMed: 26788865]
62. Zhou J, Tryggestad E, Wen Z, et al. Differentiation between glioma and radiation necrosis using molecular magnetic resonance imaging of endogenous proteins and peptides. Nat Med 2011;17:130–134. [PubMed: 21170048]
63. Jones KM, Pollard AC, Pagel MD. Clinical applications of chemical exchange saturation transfer (CEST) MRI. J Magn Reson Imaging 2018;47:11–27. [PubMed: 28792646]
64. Pereira GC, Traughber M, Muzic RF. The role of imaging in RT planning: Past, present, and future. Biomed Res Int 2014;2014: 231090. [PubMed: 24812609]
65. Gudur MS, Hara W, Le QT, et al. A unifying probabilistic Bayesian approach to derive electron density from MRI for RT treatment planning. Phys Med Biol 2014;59:6595–6606. [PubMed: 25321341]
66. Ren S, Hara W, Wang L, et al. Robust estimation of electron density from anatomical MR imaging of the brain using a unifying multiatlas approach. Int J Radiat Oncol Biol Phys 2017;97:849–857. [PubMed: 28244422]
67. Lagendijk JJ, Raaymakers BW, van Vulpen M. The magnetic resonance imaging-linac system. Semin Radiat Oncol 2014;24:207–209. [PubMed: 24931095]
68. Wong KH, Panek R, Bhide SA, et al. The emerging potential of magnetic resonance imaging in personalizing radiotherapy for head and neck cancer: An oncologist's perspective. Br J Radiol 2017;90: 20160768. [PubMed: 28256151]
69. Ahmad SB, Sarfehnia A, Paudel MR, et al. Evaluation of a commercial MRI Linac based Monte Carlo dose calculation algorithm with GEANT4. Med Phys 2016;43:894–907. [PubMed: 26843250]
70. Acharya S, Fischer-Valuck BW, Kashani R, et al. Online magnetic resonance image guided adaptive RT: First clinical applications. Int J Radiat Oncol Biol Phys 2016;94:394–403. [PubMed: 26678659]
71. Hamstra DA, Galban CJ, Meyer CR, et al. Functional diffusion map as an early imaging biomarker for high grade glioma: Correlation with conventional radiologic response and overall survival. J Clin Oncol 2008;26:3387–3394. [PubMed: 18541899]
72. Nelson SJ, Kurhanewicz J, Vigneron DB, et al. Metabolic imaging of patients with prostate cancer using hyperpolarized [1-^{13}C]pyruvate. Sci Transl Med 2013;5:198ra108.
73. Vos PC, Hambrock T, Hulsbergen-van de Kaa CA, et al. Computerized analysis of prostate lesions in the peripheral zone using dynamic contrast enhanced MRI. Med Phys 2008;35:888–899. [PubMed: 18404925]

74. Langer DL, van der Kwast TH, Evans AJ, et al. Prostate cancer detection with multi-parametric MRI: Logistic regression analysis of quantitative T2, diffusion-weighted imaging, and dynamic contrast-enhanced MRI. J Magn Reson Imaging 2009;30:327–334. [PubMed: 19629981]

75. Ozer S, Langer DL, Liu X, et al. Supervised and unsupervised methods for prostate cancer segmentation with multispectral MRI. Med Phys 2010;37:1873–1883. [PubMed: 20443509]

76. Hamilton J, Franson D, Seiberlich N. Recent advances in parallel imaging for MRI. Prog Nucl Magn Reson Spectrosc 2017;101:71–95. [PubMed: 28844222]

77. King AD, Thoeny HC. Functional MRI for the prediction of treatment response in head and neck squamous cell carcinoma: Potential and limitations. Cancer Imaging 2016;16:23. [PubMed: 27542718]

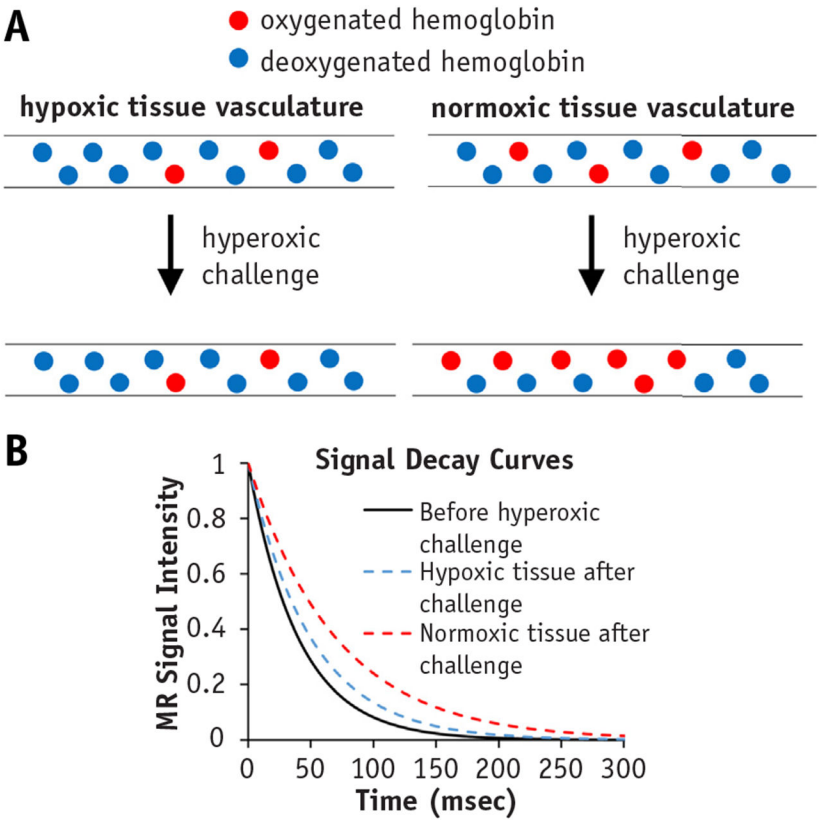

Fig. 1.

Blood oxygen level–dependent MRI. (A) Schematic of hypoxic and normoxic tissue responses to hyperoxic challenge. Hypoxic tissues show minimal change in degree of oxygenated hemoglobin (blue circles), whereas normoxic tissue vasculature is associated with increased oxygenated hemoglobin (red circles). (B) Graph of fitted MR signal intensity to multi-echo MR signal intensity data shows increased T_2* measurements in normoxic tissue (red dashed curve) after an oxygen challenge compared with T_2* measurements in hyperoxic tissue (blue dashed curve) after an oxygen challenge.

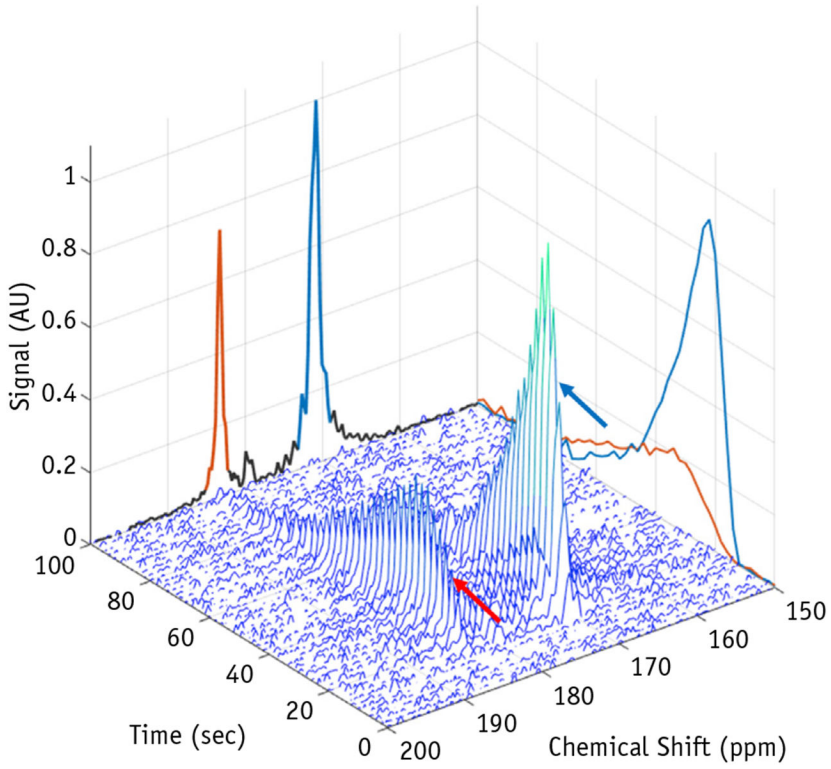

Fig. 2.

Waterfall schematic of hyperpolarized ^{13}C-pyruvate MRI. Magnetic resonance signal intensities from a range of chemical shifts (ppm) are recorded simultaneously over time. Dynamic wash-in and wash-out time curves are observed at the chemical shifts of pyruvate (171 ppm, blue arrow) and lactate (183 ppm, red arrow). These curves are typically analyzed by taking the ratio of the summation of time signal intensity data from lactate and pyruvate to measure a lactate fraction and thereby estimate the metabolic state of the tumor tissue.

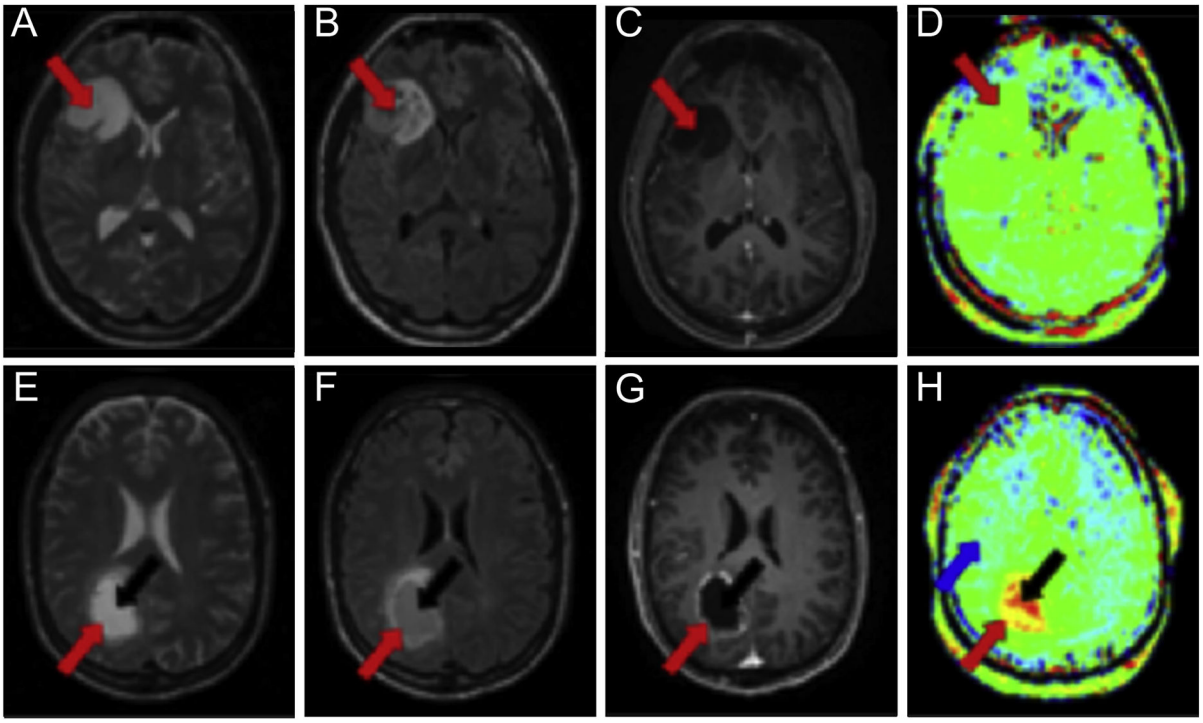

Fig. 3.

Amide proton transfer MRI of cancer. (A-D) Brain MR images from a 30-year-old female patient with low-grade oligodendroglioma; (E-H) brain MR images from a 58-year-old male patient with high-grade glioblastoma. Axial T2-weighted images (A, E) and axial fluid attenuated inversion recovery images (B, F) delineate the locations of the tumor rim (red arrow) and core (black arrow). Gadolinium-enhanced T1-weighted images (C, G) show no contrast enhancement for the low-grade tumor (C) and an enhancing rim with a nonenhancing central area for the high-grade tumor (G). Amide proton transfer–weighted images (D, H) show isointensity compared with contralateral brain tissue for the low-grade tumor (D) and hyperintensity compared with normal brain tissue (blue arrow) for the high-grade tumor (H). Adapted with permission from reference (56).

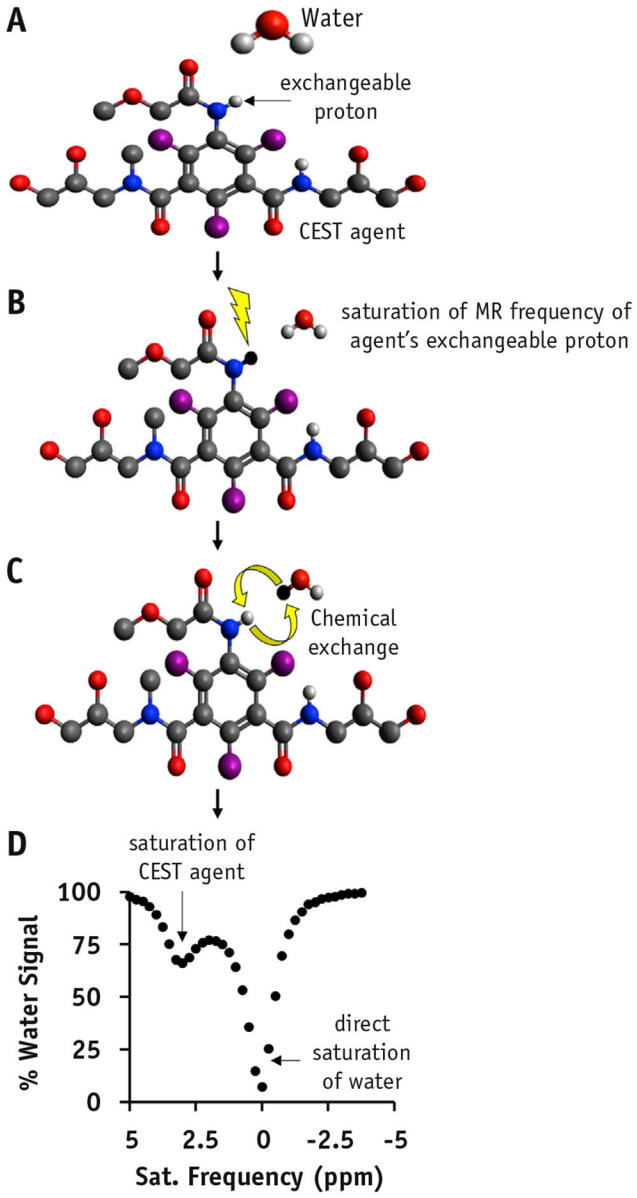

Fig. 4.

Chemical exchange saturation transfer (CEST) mechanism. (A) An endogenous molecular agent with an exchangeable proton can be detected with CEST by saturating the exchangeable proton (lightning bolt in B), thus allowing for exchange of the proton with water (C) and subsequently acquiring a CEST spectrum (D).

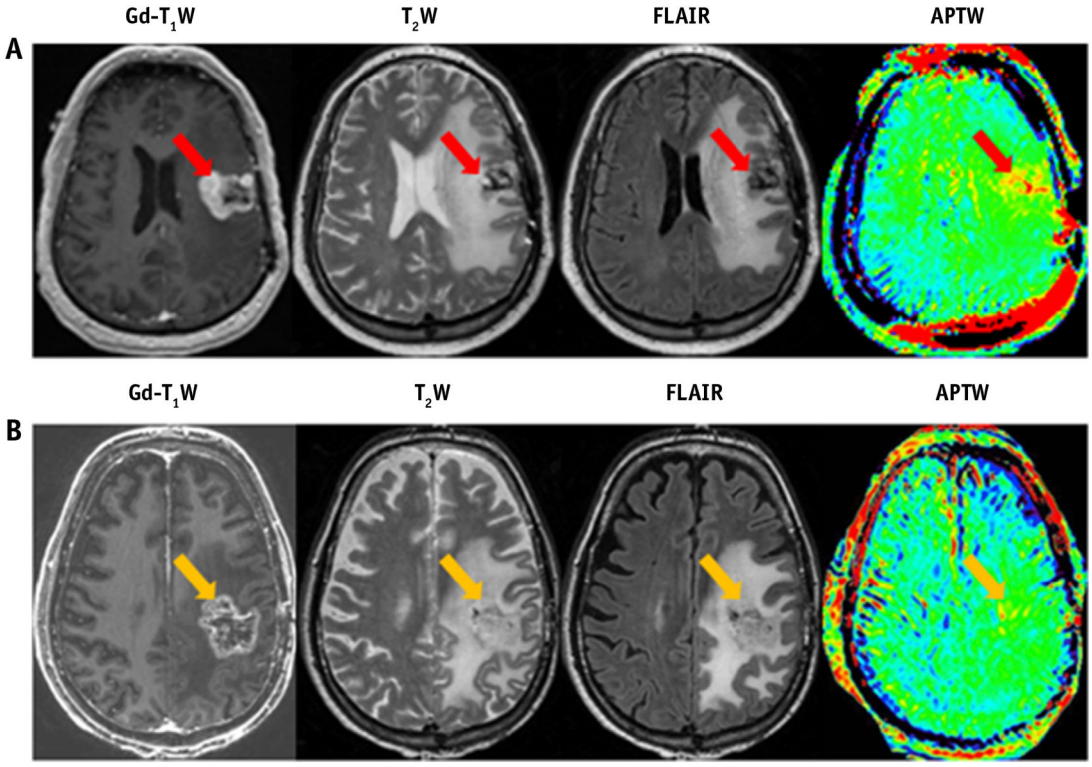

Fig. 5.

Conventional and amide proton transfer–weighted (APTW) MRI from a 49-year-old man with tumor progression (A) and from a 65-year-old man with a clinical diagnosis of pseudoprogression (B). Patient A, with pathologically proved glioblastoma, had undergone resection and chemoradiation and developed a new contrast-enhancing lesion 1 month after completion of chemoradiation. Patient B, with pathologically proven glioblastoma, had undergone resection and chemoradiation and developed a new contrast-enhancing lesion 3 months after chemoradiation. Adapted with permission from reference (61).

Table 1

Clinical experience with established and emerging MRI techniques for radiation therapy response assessment

Imaging technique*	Tissue properties measured	In-plane resolution (mm^2)	Slice thickness (mm)	All published studies	Published studies in assessing radiation treatment response
T_1-W, T_2-W MRI	Tumor delineation	0.5-2	2-5	+++++	+++++
DW MRI	Cellularity	2-3	4-6	++++	++++
DCE MRI	Permeability, perfusion	2-3	4-6	++++	++++
MR spectroscopy	Metabolite concentrations	6-20	10-25	++	++
BOLD MRI	Oxygenation	2-4	3-6	+++	+
CEST MRI	Protein concentrations	2-3	2-6	+++	+++
Hyperpolarized ^{13}C MRI	Pyruvate metabolism	7-15	10-20	+	+

Abbreviations: BOLD = blood oxygenation level–dependent; CEST = chemical exchange saturation transfer; DCE = dynamic contrast-enhanced; DW = diffusion-weighted; T_1 = T_1-weighted; T_2-W = T_2-weighted.

+++++ = widespread clinical use. ++++ = published literature in a variety of tissue types; becoming widespread clinically. +++ = emerging technique with demonstrated clinical success in some tissues. ++ = older technique with limited success clinically. + = emerging technique with published experience limited to small animal imaging.

*Parameters for standard T_1-W MRI, T_2-W MRI, DW MRI, DCE MRI, MR spectroscopy, BOLD MRI, and CEST MRI are summarized with input from an experienced clinical medical physicist (R. Jason Stafford, PhD). The listed spatial resolution and slice thickness for hyperpolarized MRI is as summarized in previous published clinical work in patients with prostate cancer (72).